Electronic Supplementary Material (ESI) for Energy & Environmental Science.

Sublayer-enhanced atomic sites of single atom catalysts through in-situ atomization of metal oxide nanoparticles

Xing Wu[#a], Qichen Wang[#b], Shize Yang[#c], Jinyang Zhang[#d], Yi Cheng[a]*, Haolin Tang[e], Lu Ma[f], Xiaobo Min[a]*, Chongjian Tang[a], San Ping Jiang[g], Feixiang Wu[a], Yongpeng Lei[b], Simone Ciampic[d], Shuangyin Wang[h], Liming Dai[i]*

[a] Institute of Environmental Science and Engineering, School of Metallurgy and Environment, Central South University, Changsha 410083, P.R. China Address here.

[b] State Key Laboratory of Powder Metallurgy, Central South University, Changsha 410083, P.R. China.

[c] Eyring Materials Center, Arizona State University, Tempe, AZ 85257, United States.

[d] School of Molecular and Life Sciences, Curtin Institute of Functional Molecules and Interfaces, Curtin University, Bentley, Western Australia 6102, Australia.

[e] Foshan Xianhu Laboratory of the Advanced Energy Science and Technology Guangdong Laboratory, Xianhu Hydrogen Valley, Foshan, 528216 China.

[f] Brookhaven National Laboratory, National Synchrotron Light Source II Bldg. 743 P.O. Box 5000, Upton, NY 11973-5000.

[g] WA School of Mines: Minerals, Energy and Chemical Engineering, Curtin University, Perth, WA 6102, Australia.

[h] State Key Laboratory of Chem/Bio-Sensing and Chemometrics, Provincial Hunan Key Laboratory for Graphene Materials and Devices, College of Chemistry and Chemical Engineering, Hunan University, Changsha, 410082 China.

[i] Australian Carbon Materials Centre(A-CMC), School of Chemical Engineering, University of New South Wales, Sydney, NSW2052, Australia.

Experimental Section

1.1 Materials synthesis

The graphene adopted in present study was obtained from the Institute of Coal Chemistry, Chinese Academy of Sciences (single layer with average thickness of 0.4 nm). The as-received graphene was purified following the procedure reported. The purified graphene was functionalized with PEI, and the PEI functionalized graphene (100 mg) was firstly ultrasonicated in 100 mL EG solution for 1 h, followed by the addition of iron (III) acetylacetonate. The dispersion was ultrasonicated for 15 min and then stirred for another hour before being placed in a three-neck bottle and heated for 5 min, followed by stirring overnight. The solution was then filtered using a nylon membrane and washed for several times. Similarly, the CoO_x was synthesized as well with the aim to demonstrate the universal trend.

FeO_x/G (10 mg) was dispersed in 20 mL ethanol under ultrasonic for 30 min before being mixed with $C_2H_4N_2$ (10 g) by grinding till the mixture was dried. Subsequently, the mixed powder was heated at 350 ◦C for 3 h and then at 650 ◦C for 3 h before being heated at 900 ◦C for 1 h under Ar with a flow rate of 50 mL min^{-1}. The obtained products are washed with acid and then the iron content was tested adopting inductively coupled plasma - optical emission spectrometer (ICP-OES), and denoted as X-FeSA (X is the actual loading of the iron).

1.2. Characterization

The obtained materials were firstly analysed by X-ray powder diffraction. The morphology of the catalysts was studied by scanning electron microscopy (SEM), transmission electron microscopy (TEM) and high angle annular dark field (HAADF) scanning TEM (STEM) with elemental mapping on a Titan G2 60-300 at 80 kV. The annular dark field images (ADF) were collected using a Nion UltraSTEM100 microscope operated at 60 kV at a beam current of 60 pA. The convergence half angle of the electron beam was set to 30 mrad and the inner collection half angle of the ADF images was 51 mrad. Diffraction data was collected with a Bruker D8 Advance diffractometer operated at 40 kV and 40 mA with Cu Kα (λ = 1.5406 Å) in the range of 20-90◦ 2θ. X-ray photoelectron spectroscopy (XPS) were conducted on a Kratos Axis Ultra DLD spectrometer using a monochromatic AlKα (1486.6 eV) irradiation source operated at 225 W.

X-ray absorption spectroscopy (XAS) measurements were performed at the wiggler XAS Beamline (12ID) at the Australian Synchrotron in Melbourne, Australia using a set of liquid nitrogen cooled Si (111) monochromator crystals. With the beamline optics employed (Si-coated collimating mirror and Rh-coated focussing mirror) the harmonic content of the incident X-ray beam was negligible. XAS measurements were performed at the Fe K-edge (7.1 keV) at < 10 K to minimize thermal disorder and to ensure that the samples were not radiation damaged (This was confirmed via repetitive quick scanning of the absorption edge for up to 2 h, i.e., 12 scans. Note that a single complete XAS scan took ~1 h). For these samples were prepared as pellets via mechanical grinding in a cellulose binder using a mortar/pestle. Both fluorescence and transmission

spectra were recorded depending on the concentration of Fe in each sample (the validity of this approach was confirmed by comparing the fluorescence and transmission spectrum for one of the samples for which both methods yielded comparable signal-to-noise data).

1.3 Electrochemical characterization

Electrochemical measurements were conducted in an electrochemical station of Auto Lab in a typical three-electrode system. Graphite rod and Ag/AgCl (saturated KCl) electrode with electrolytic bridge were used as the counter and reference electrodes. The catalysts materials (4 mg) were ultrasonically mixed in 1 mL of ethanol nafion mixture (with Ethnol: Nafion 19:1) to form a homogeneous ink, followed by dropping certain amount of active material ink onto the surface of rotating disk electrode (RDE, 0.19625 cm^{-2}). The X-FeSA catalyst loading was ~0.408 mg cm^{-2}, and Pt loading was ~0.2 mg cm^{-2} for Pt/C. Linear scan voltammetry (LSV) curves of X-FeSA and Pt/C (20 % Pt, JM) were obtained in N_2 or O_2-saturated 0.1 M KOH or 0.1 M $HClO_4$ solution using RDE with rotating rate of 1600 rpm. The IR-corrected Tafel plots were recorded at a scan rate of 1 mV s^{-1}. All potentials in the present study were given versus RHE reference electrode (E = E^{0}_{AgCl}+0.197+ 0.059 pH, here 0.197 V is the potential for Ag/AgCl at 20 ◦C). The electron transfer number (n) of catalysts was calculated through the Koutecky–Levich (K–L) equations:

$$\frac{1}{J}=\frac{1}{J_L}+\frac{1}{J_K}=\frac{1}{Bw^{1/2}}+\frac{1}{J_K} \qquad (1)$$

$$B = 0.62nFD_0^{2/3}v^{-1/6}C_0 \quad (2)$$

where J, J_L, and J_k is the measured, diffusion-limiting, and the kinetic current density, respectively. ω is the electrode-rotating angular velocity, F is the Faraday constant (96485 C mol^{-1}), D_o represents the diffusion coefficient of O_2 and is 1.9×10^{-5} cm^2 s^{-1} in 0.1 M KOH, ν represents kinetic viscosity of the electrolyte and is 0.01 cm^2 s^{-1}, and Co represents the density of O_2 and is 1.2×10^{-6} mol cm^{-3}.

Moreover, The H_2O_2 yield and the electron transfer number are calculated from the LSV of rotating ring disk electrode (RRDE, 0.2475 cm^{-2}) measurement at 1600 rpm according to the formulas:

$$H_2O_2\% = \frac{200\frac{I_R}{N}}{(\frac{I_R}{N} + I_D)} \quad (3)$$

$$n = \frac{4I_D}{N(\frac{I_R}{N} + I_D)} \quad (4)$$

Where I_D and I_R is the disk current and the ring current, respectively. N is the collection efficiency (37%) and n is the electron transfer number.

1.4 Quantification of the active sites.

The SD and turnover frequency were obtained according to the method presented by Shui et al.[1] Briefly, extensive cycling in pH 5.2 acetate buffer alternatively in O_2 and N_2 was performed to obtain nonchanging cyclic voltammetry curves in N_2. Then the catalyst was poisoned by $NaNO_2$. The ORR performance was recorded before, during

and after the nitrite absorption. Nitrite stripping was conducted in the region of 0.7 to −0.5 V versus the reversible hydrogen electrode. The excess in cathodic charge (Q_{strip}) was proportional to the SD, and the turnover frequency was calculated by dividing the difference of kinetic current before and after nitrite absorption by SD:

$$SD(mol\ g^{-1}) = \frac{Q_{strip}(C\ g^{-1})}{n_{strip}F(C\ mol^{-1})} \quad (5)$$

$$TOF(s^{-1}) = \frac{n_{strip}\Delta j_k(mA\ cm^{-2})}{Q_{strip}L_c(mA\ cm^{-2})} \quad (6)$$

where n_{strip} (= 5) is the number of electrons associated with the reduction of one nitrite per site, $j_k = \frac{j_{lim} \times j}{j_{lim} - j} is\ the\ kinetic\ current\ density$, where j_{lim} was taken as the current density achieved @0.2V versus RHE, L_C is the catalyst loading (0.27 mg cm^{-2}).

1.5 DTF calculations

The density functional theory (DFT) calculations were carried out employing the VASP[2, 3] within the generalized gradient approximation (GGA) using the Perdew-Burke-Ernzerhof (PBE)[4] formulation. The projected augmented wave (PAW) potentials[5] have been chosen to describe the ionic cores. Take valence electrons into account using a plane wave basis set with a kinetic energy cutoff of 520 eV. Partial occupancies of the Kohn-Sham orbitals were allowed using the Gaussian smearing method and a width of 0.05 eV. The electronic energy was considered self-consistent

when the energy change was smaller than 10^{-5} eV. A geometry optimization was considered convergent when the energy change was smaller than 0.03 eV/Å. The brillouin zone is sampled with 3 × 3 × 1 Monkhorst mesh.[6] Gibbs free energy can be obtained by adding corrections including entopic (*TS*) and zero-point energy (ZPE) to calculated DFT energy, so that $\Delta G = \Delta E_{DFT} + \Delta ZPE - T\Delta S - eU$. where the E_{DFT} is the calculated DFT reaction energy, ΔZPE is the change in ZPE calculated from the vibrational frequencies and Δ*S* is the change in the entropy referring to thermodynamics databases. The electrode potential is adopted with respect to the reversible hydrogen electrode, which makes the standard electrochemical potential of electron involved in reaction (G_e) equal to -e*U*, and the standard electrochemical potential of the proton (G_{H+}) equal to that of the hydrogen atom in gaseous H_2 ($1/2G_{H2}$). Considering that the triplet state of the O_2 molecule is poorly described in the current DFT scheme, the free energy of the O_2 molecule was derived according to $G_{O2} = 2G_{H2O} - 2G_{H2} + 4.92$.

1.6 Zn-air battery and Fuel cell

1.6.1 Zn-air battery

Aqueous ZABs measurement. The aqueous Zn-air battery was assembled using a home-made two electrode device, in which the self- assembled sandwich-like structure electrode, made up of catalyst layer (1.0 cm × 1.0 cm cm^{-2}), water-proof breathable membrane and Ni foam layer, was adopted as the air cathode and a polished Zn plate (purity 99.9 wt%, 0.3 mm thickness) was used as the anode. The catalyst layer was prepared by sufficiently mixed catalyst (60 mg), acetylene black (10 mg) and the

polytetrafluoroethylene (PTFE) emulsion (60 wt%, 40 μL) in ethanol solution. Then, the catalyst layer was cut into 1.0 cm × 1.0 cm cm^{-2} pieces after removing excess ethanol at room temperature, and combined with water-proof breathable membrane and Ni foam layer form sandwich structure by roller press. 6M KOH + 0.2M $Zn(Ac)_2$ was used as electrolyte and applied in rechargeable ZABs. Meanwhile, the commercial Pt/C or Pt/C+RuO_2 catalyst was also used as air electrode for comparison. The galvanostatic curves (LSVs, scan rate of 5mV S^{-1}) and the rate performance and discharge-charge cycling (10 min discharge, 1 min shelving, 10 min charge followed by 1 min shelving) stability were recorded by NEWARE testing system. Both the current density and power density were normalized to the effective surface area of air electrode.

Quasi-solid-state ZABs measurement. The structure of quasi-solid-state ZABs the same as that of aqueous ZABs, which are typical sandwich-like structures. The variation is that the as-prepared air electrode and Zn plate were placed on the two sides of PAM-based gel electrolyte. Moreover, the stack pressure was employed for maintain good interfacial contact during battery measurement.

1.6.2 Fuel cell test

The performance of fuel cells was tested on a fuel cell fixture from Hephas Energy. Anhydrous H_2 (Industrial, BOC) and O_2 (High Purity, BOC) were fed to the fuel cell at a flow rate of 150 sccm and 100 sccm, respectively. Electrochemical measurements were conducted in a standard electrochemical cell using a Princeton potentiostat (Versastat3，USA). Pt foil (3.0 cm^2) and saturated calomel electrode (SCE) with electrolytic bridge were used as the counter and reference electrodes, respectively.[7]

Membrane-electrode assemblies (MEAs) with an active area of 4 cm^2 were fabricated by sandwiching the phosphoric acid doped membrane between two pieces of gas diffusion electrodes with Pt/C anode and cathode followed by hot-pressing at 4.9 MPa and 180 ^oC for 10 minutes. The performance of PA/PBI/SiO_2-based membrane cells was measured at 230 ^oC using a fuel cell fixture from Hephas Energy. Hydrogen (Industrial, BOC) at a flow rate of 100 mL min^{-1} and oxygen (High Purity, BOC) at a flow rate of 100 mL min^{-1} were supplied to the anode and cathode of the cell, respectively. Stability test of cells was undertaken at a cell voltage of 0.5 V and 160 °C using a flow rate of 100 mL min^{-1} for H_2 in the anode and 100 mL min^{-1} for oxygen in the cathode. For comparison, a fuel cell using Pt on both anode and cathode with Pt loading of 1.0 mg_{Pt} cm^{-2} has been assembled and tested following the same procedure.

2 Supplementary Figures and Tables

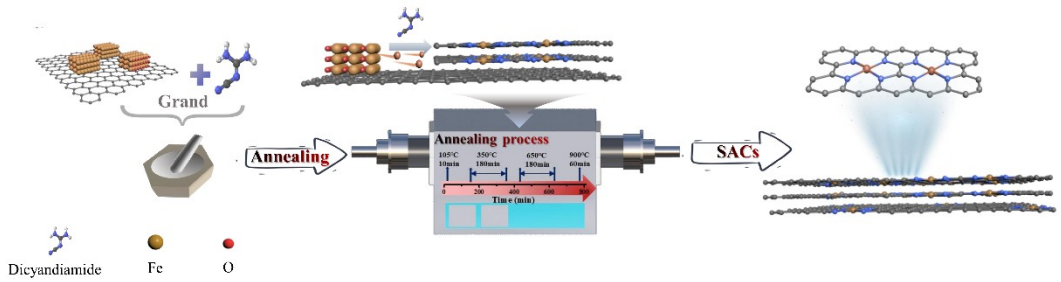

Schematic S1. A schematic illustration of synthetic route of the FeSA.

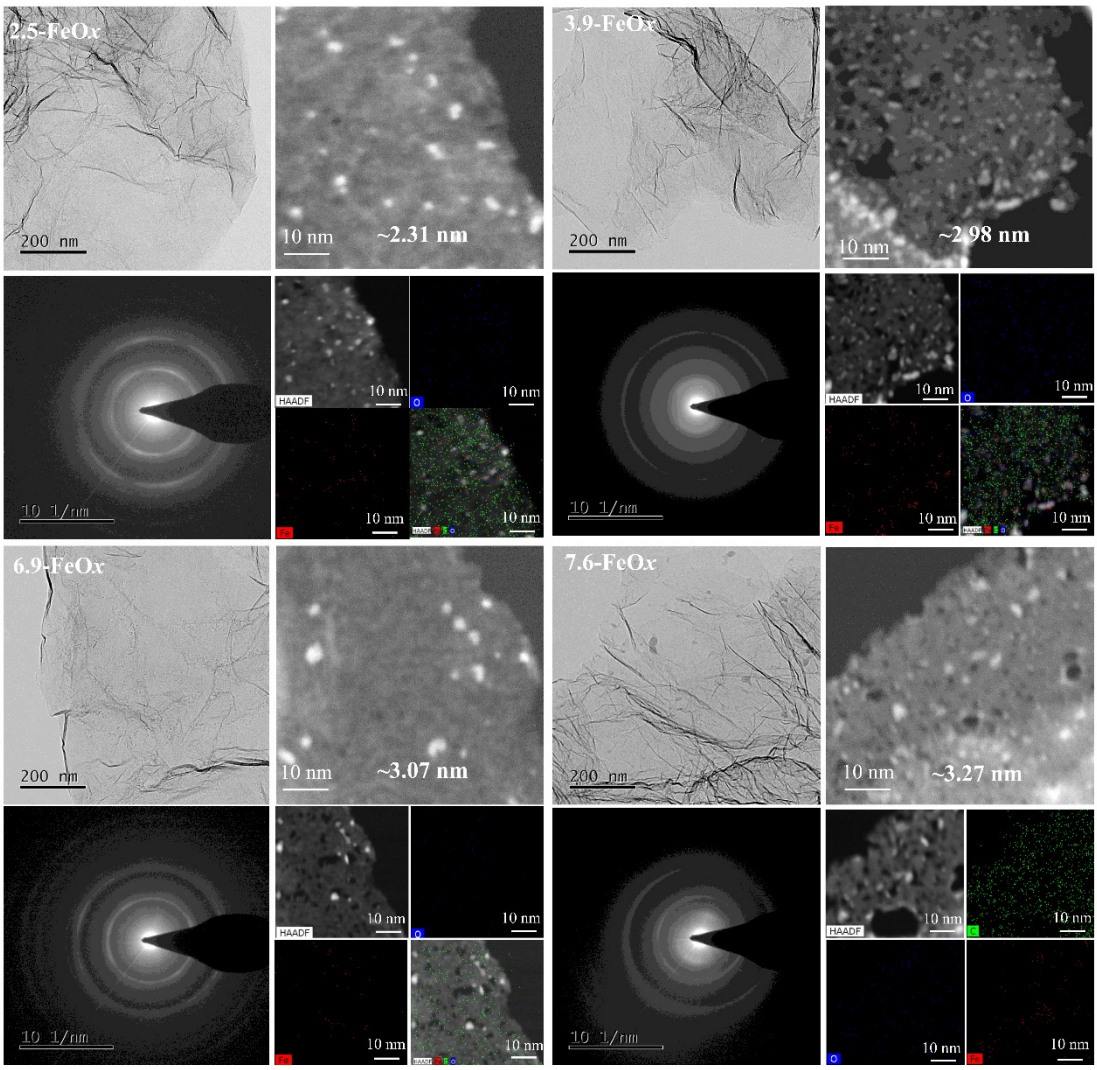

Fig. S1. The TEM image of FeO*x*.

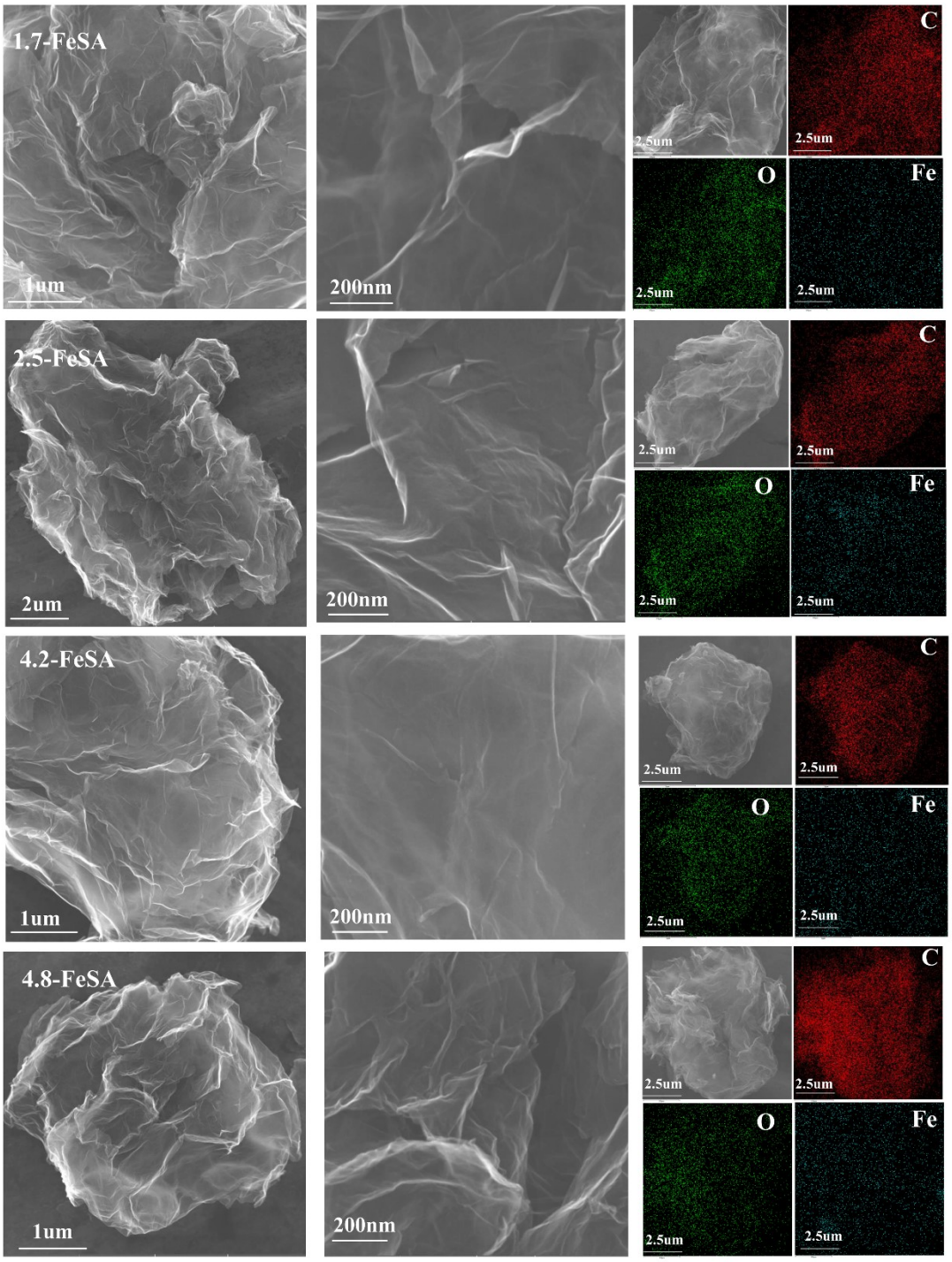

Fig. S2. The SEM image of FeSA

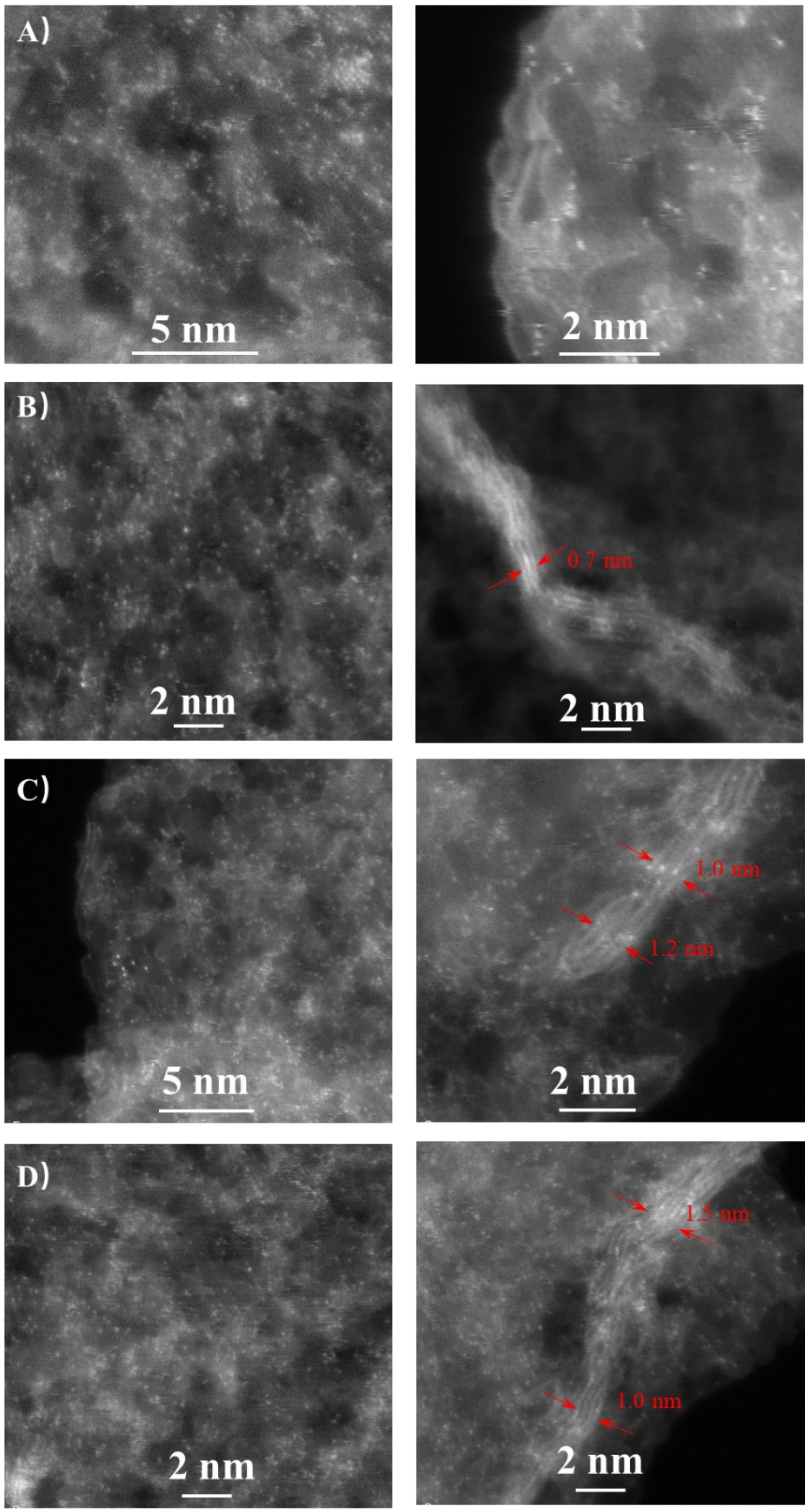

Fig. S3. The AC-TEM image of 2.5-FeSA, 5-FeSA, 10-FeSA and 20-FeSA.

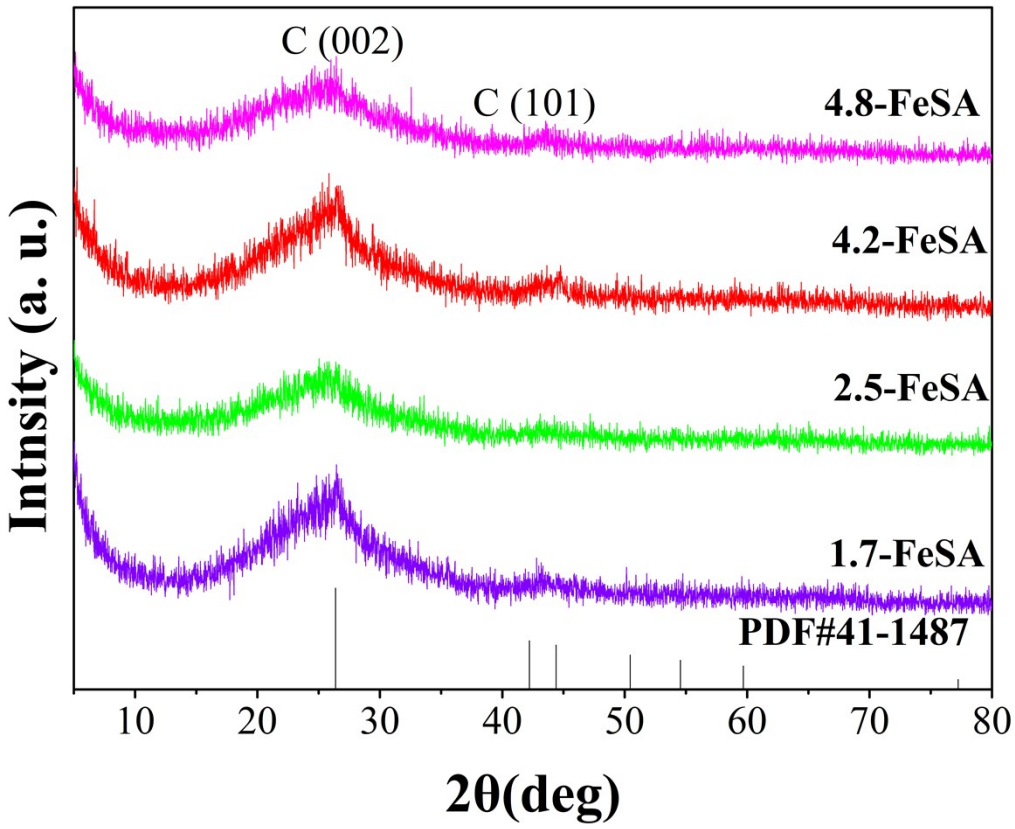

Fig. S4. The XRD of FeSA.

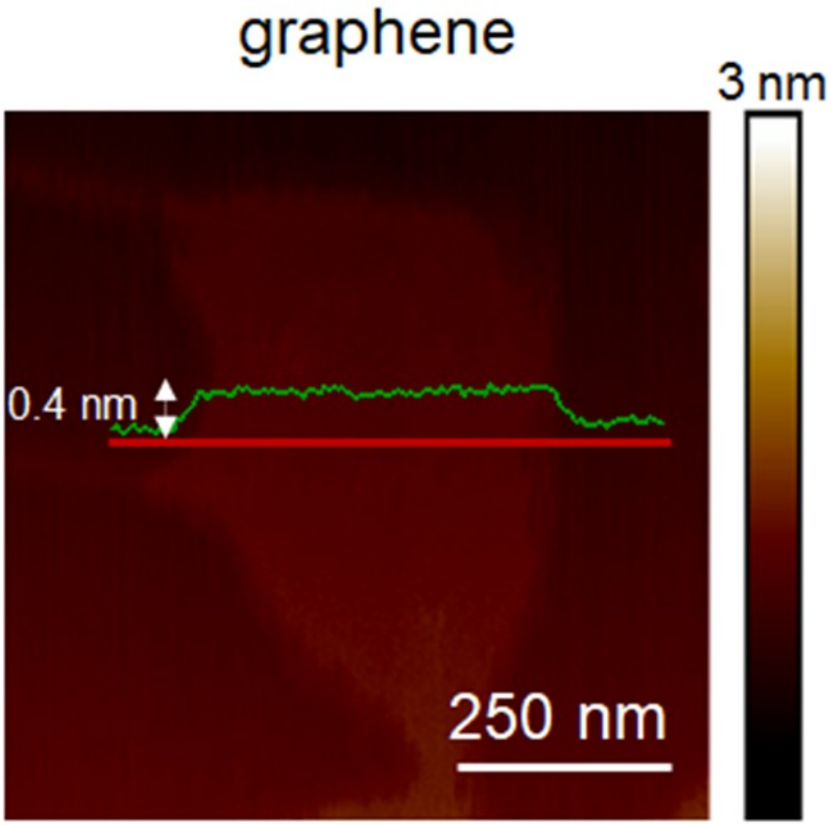

Fig. S5 The AFM image of the pristine graphene.

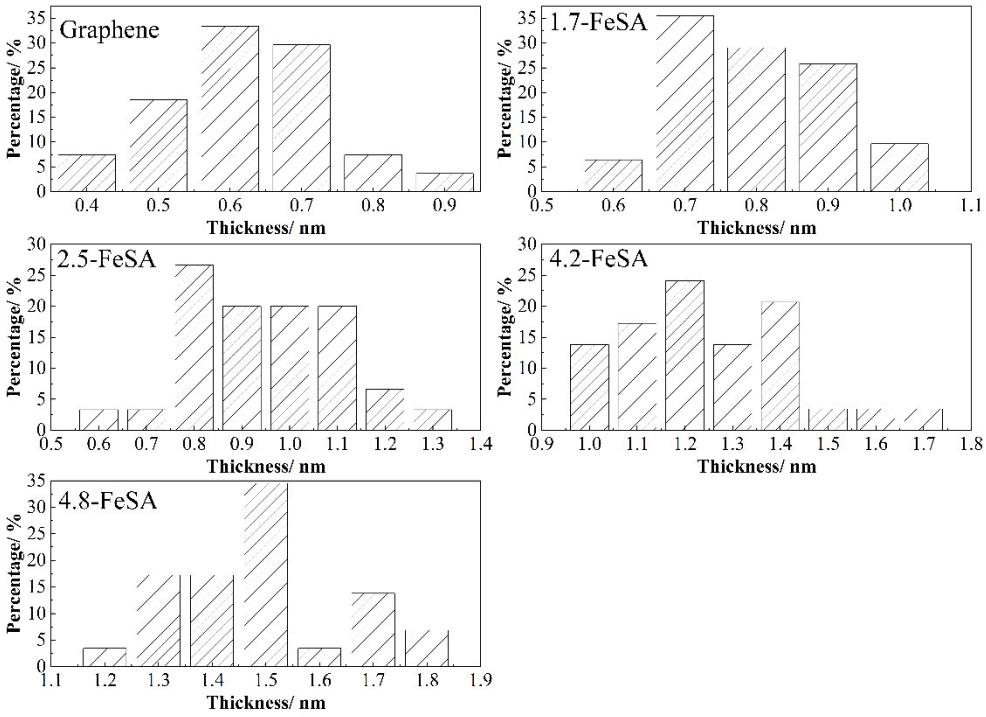

Fig. S6 The thickness of the graphene sheets before and after supported with single atoms.

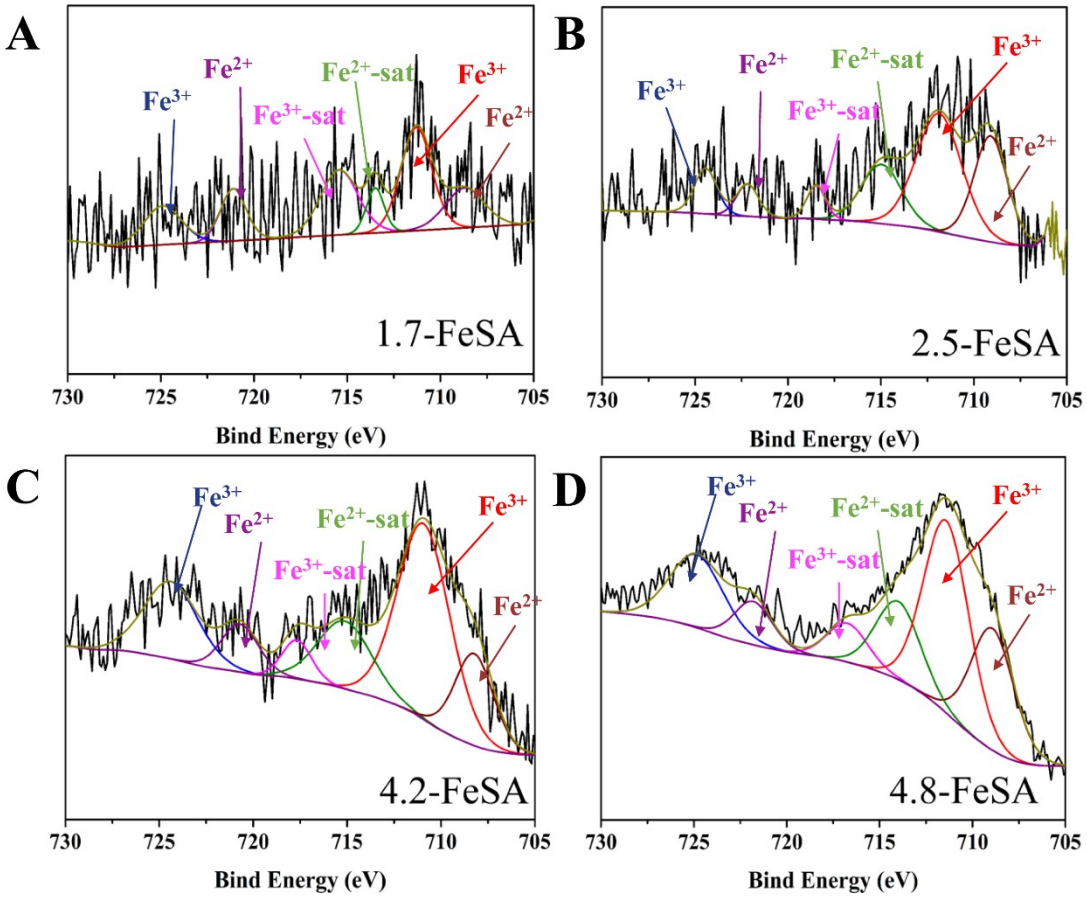

Fig. S7. The Fe 2p high resolution XPS spectra of FeSA (A-1.7-FeSA; B-2.5-FeSA; C-4.2-FeSA; D-4.8-FeSA)

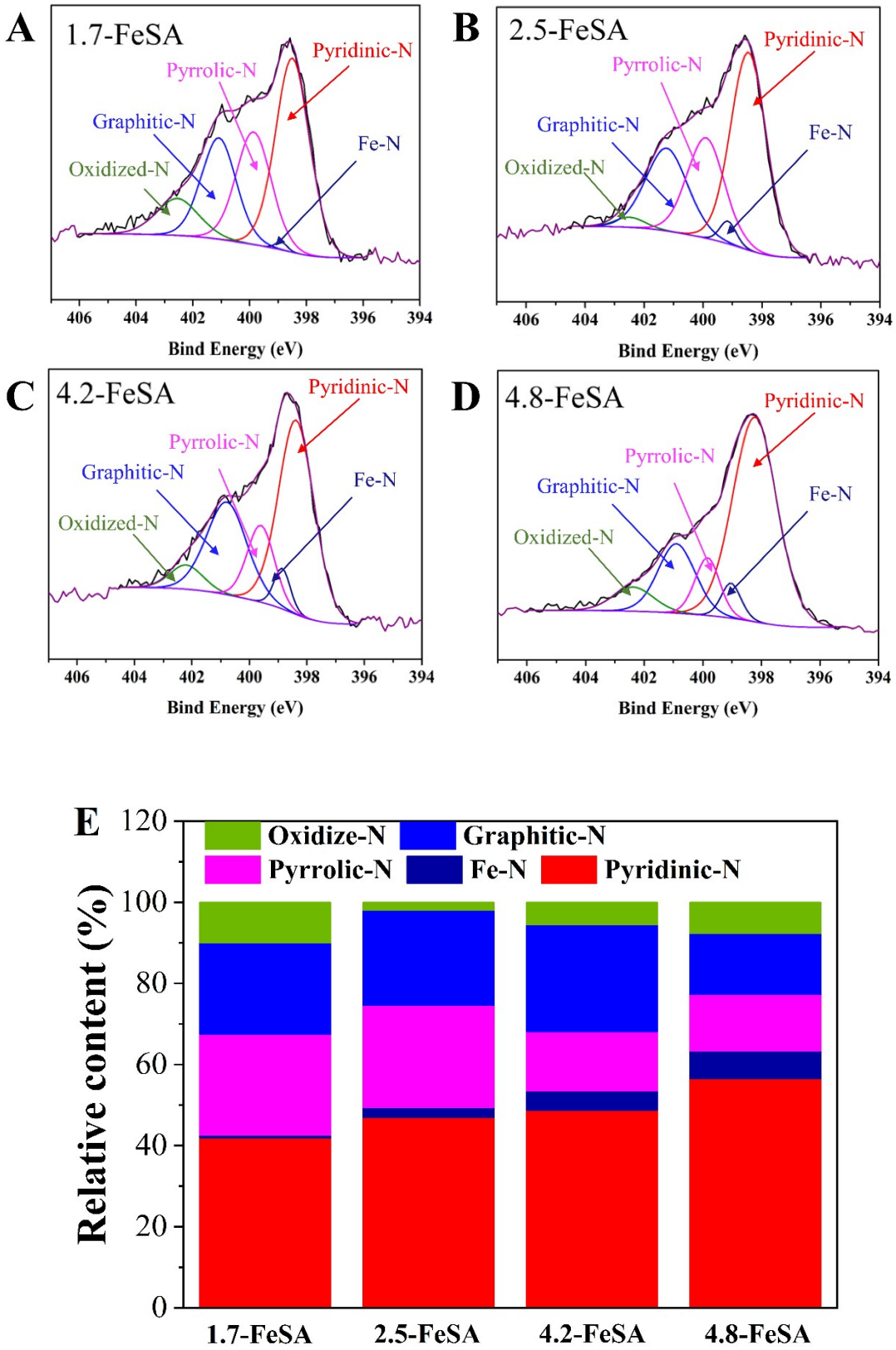

Fig. S8. The N 1s high resolution XPS spectra of FeSA (A-1.7-FeSA; B-2.5-FeSA; C-4.2-FeSA; D-4.8-FeSA), and the N relative content (%) of FeSA (E).

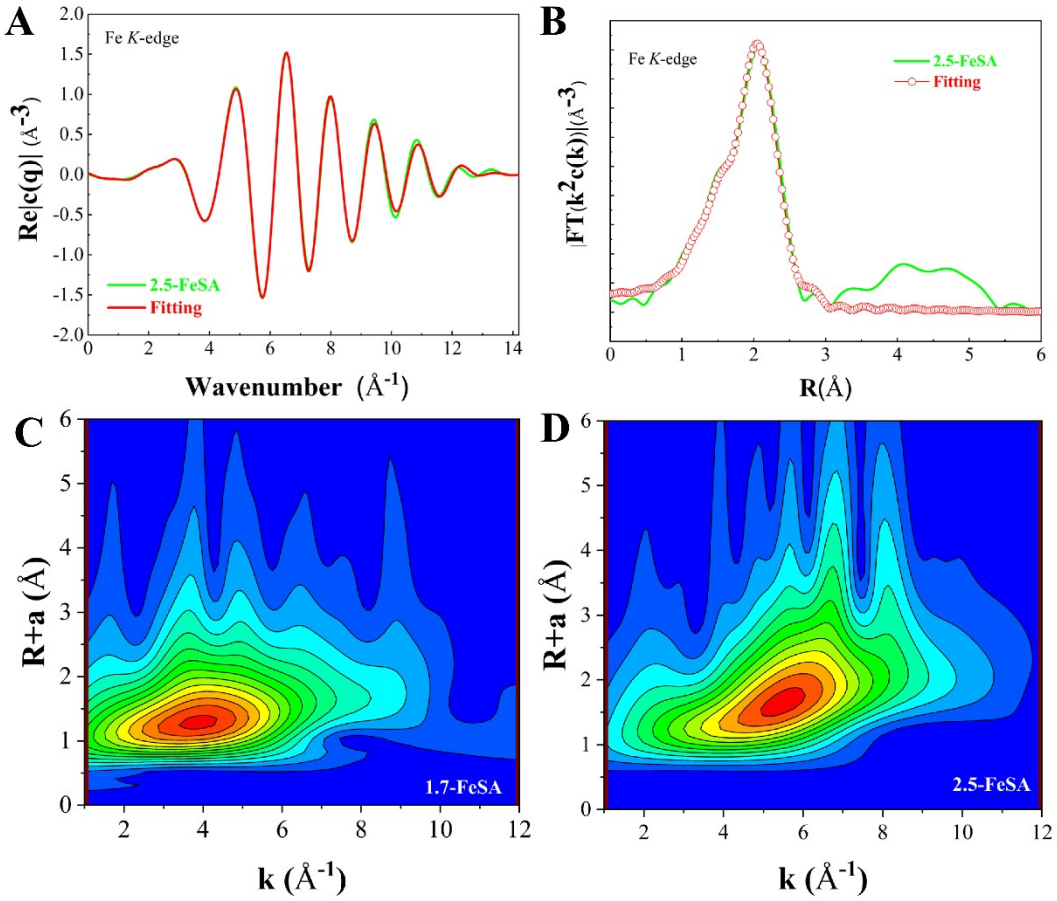

Fig. S9. Fitting results of the EXAFS spectra of 2.5-FeSA at R space (A) and K space (B), respectively. WT of the Fe K-edge of 1.7-FeSA (C) and 2.5-FeSA (D).

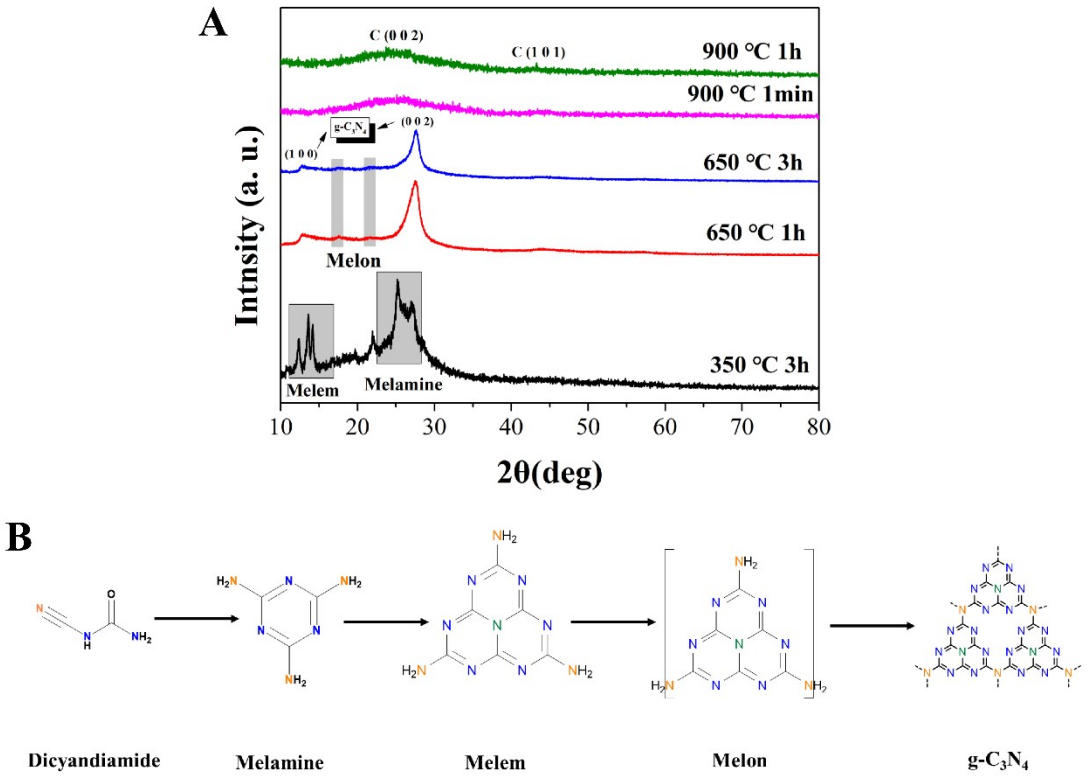

Fig. S10. The XRD results of 10-FeSA with different temperature (A) and the transformation of dicyandiamide in this experiment (B).

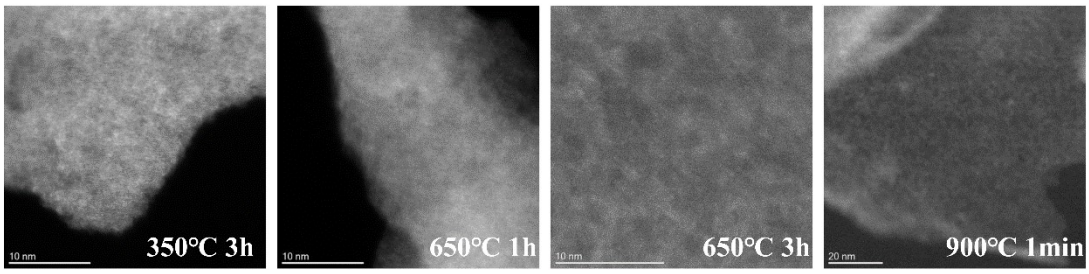

Fig. S11. The AC-STEM image of 4.2-FeSA at different temperature.

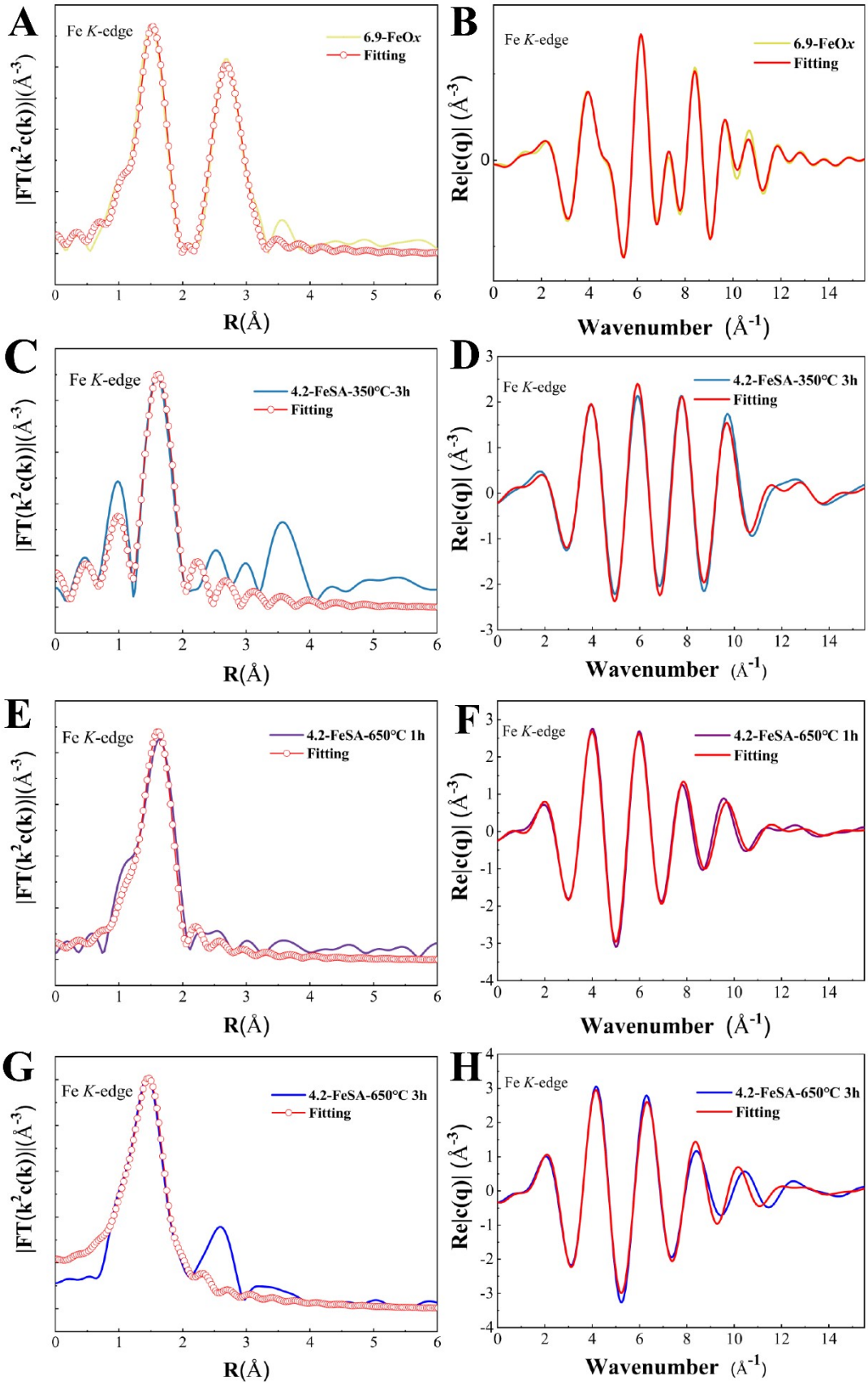

Fig. S12. In the process of pyrolysis, fitting results of the EXAFS spectra of 4.2-FeSA at R space (A, C, E, G) and K space (B, D, F, H), respectively

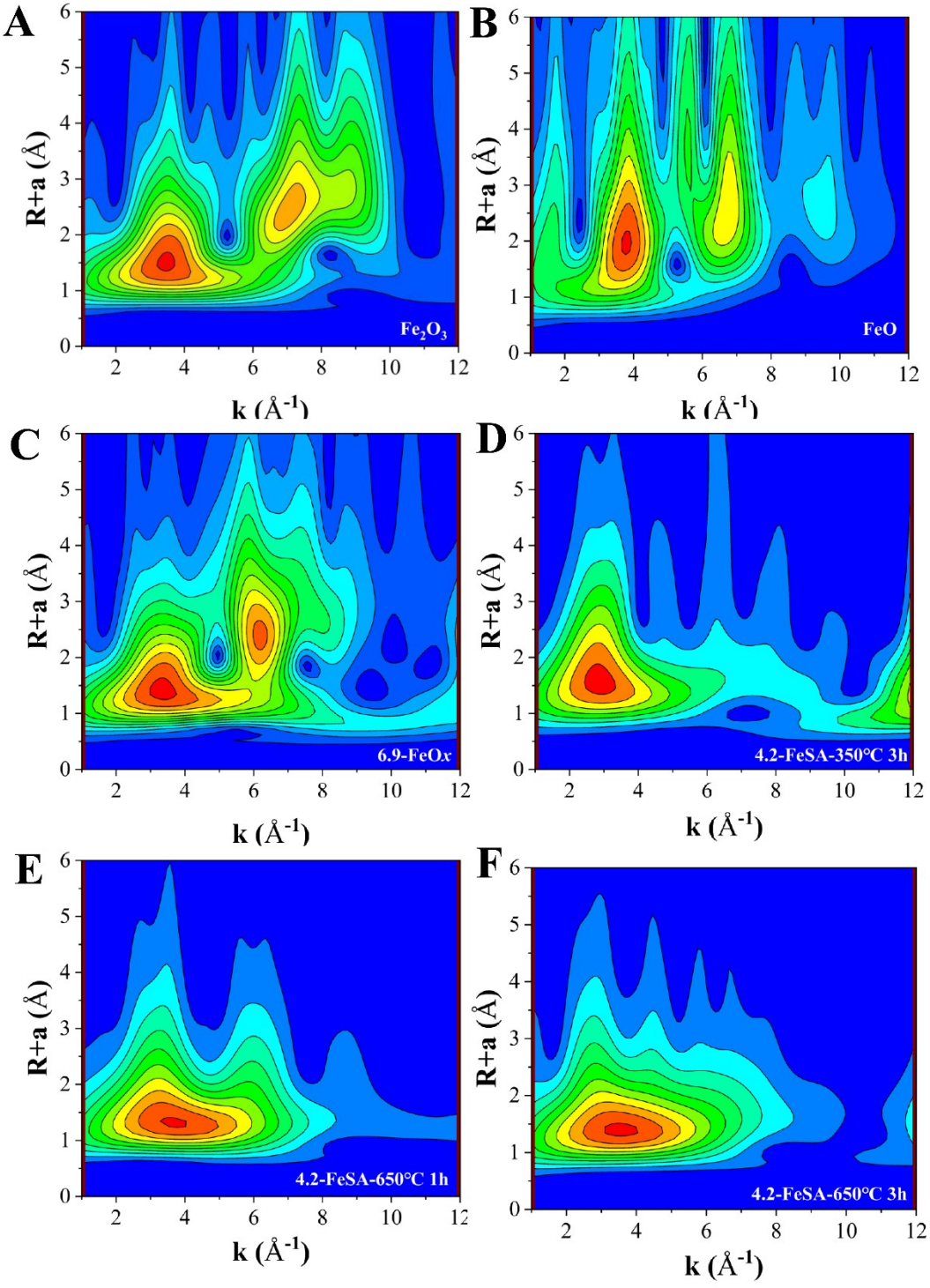

Fig. S13. In the process of pyrolysis, WT of the Fe K-edge of 4.2-FeSA, referenced Fe_2O_3 and FeO.

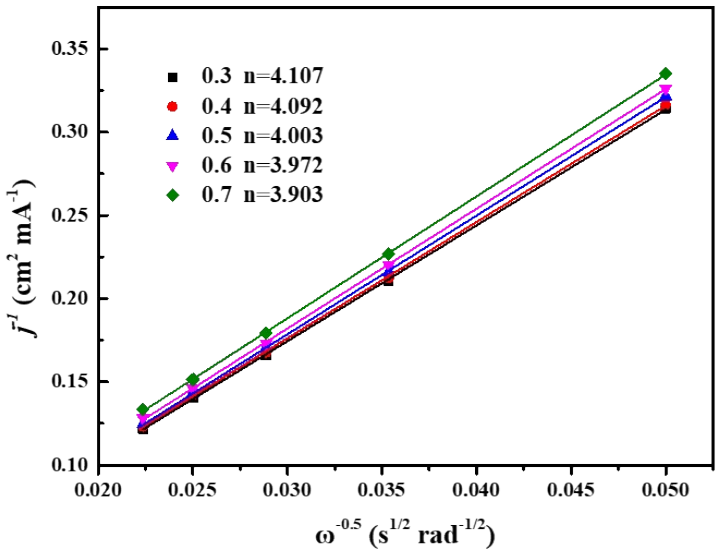

Fig. S14. The Koutecky-Levich (K-L) of 4.2-FeSA at potential 0.3, 0.4, 0.5, 0.6 and 0.7 V.

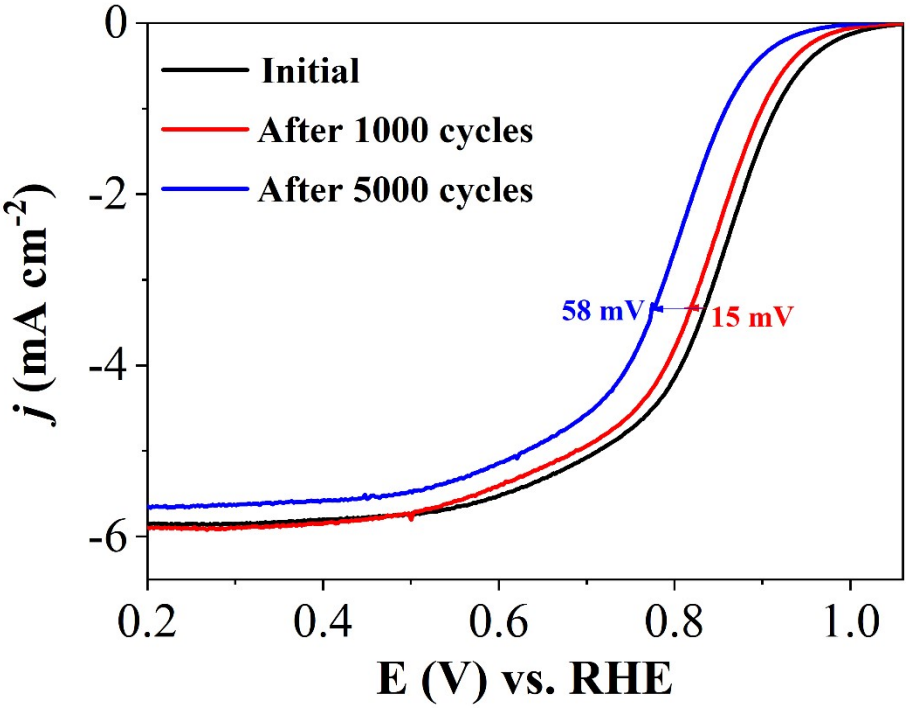

Fig. S15 RDE polarization curves of Pt/C before and after 1,000 and 5,000 cycles of accelerated durability testing

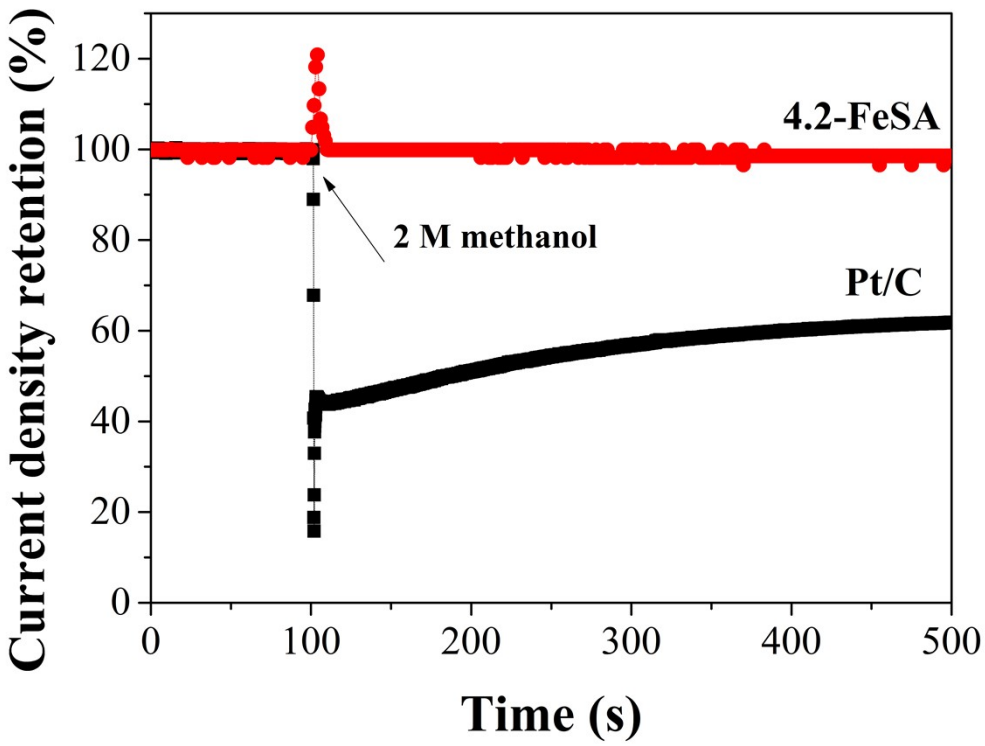

Fig. S16 Current density retention curves of 4.2-FeSA and Pt/C at 0.3 V in 0.1 m KOH with re-addition of 2 M methanol.

Fig. S17 Photograph of aqueous (A) and quasi-solid-state (B and C) Zn-air batteries.

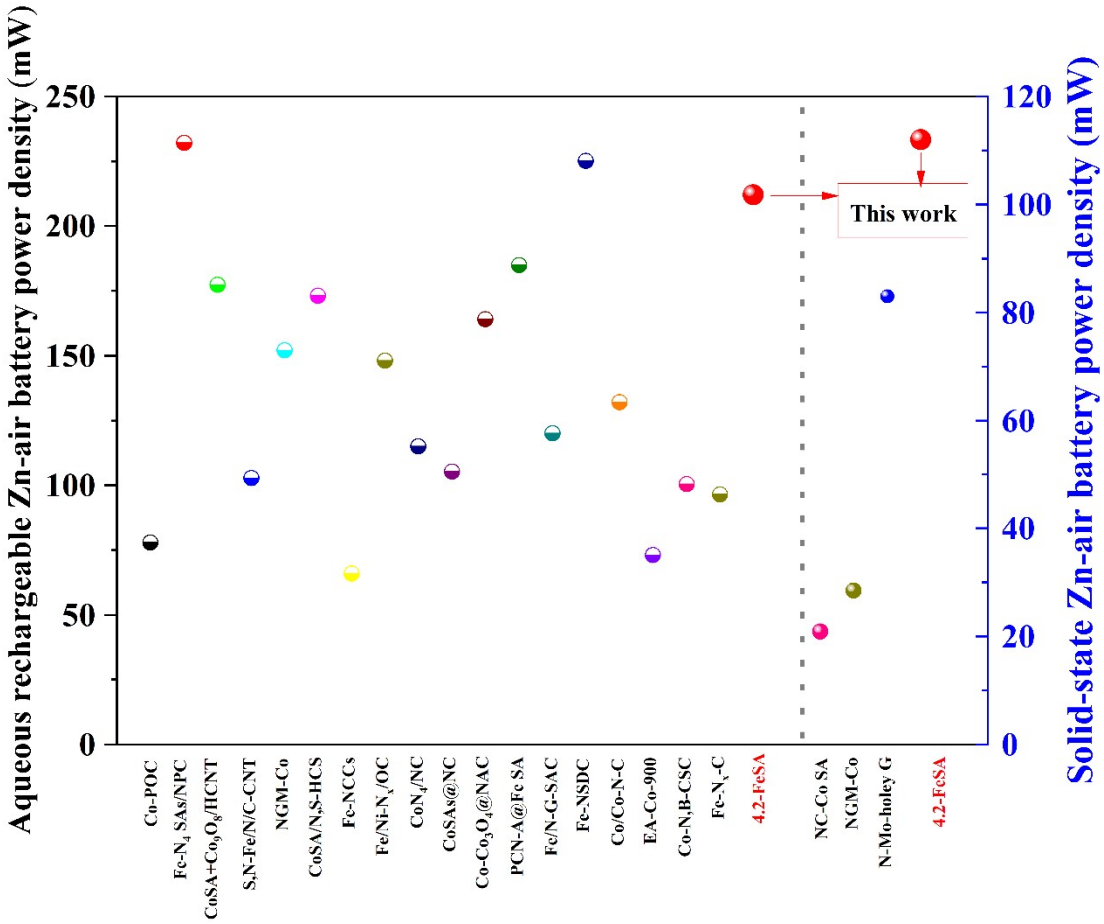

Fig. S18. The Maximum power density of 4.2-FeSA comparison with previous works.

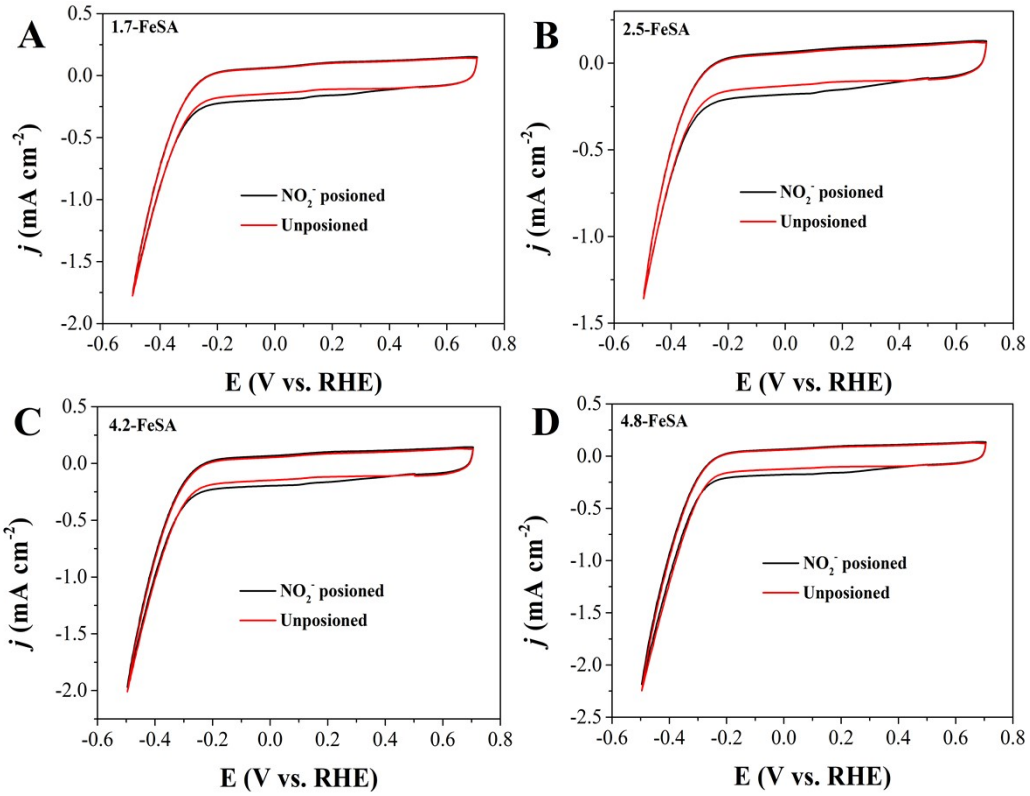

Fig. S19 Determination of site density and turnover frequency of FeSA through reversible nitrite poisoning. CV curves before and during nitrite adsorption in the nitrite reductive stripping region in a 0.5 M acetate buffer at pH 5.2 (A-D).

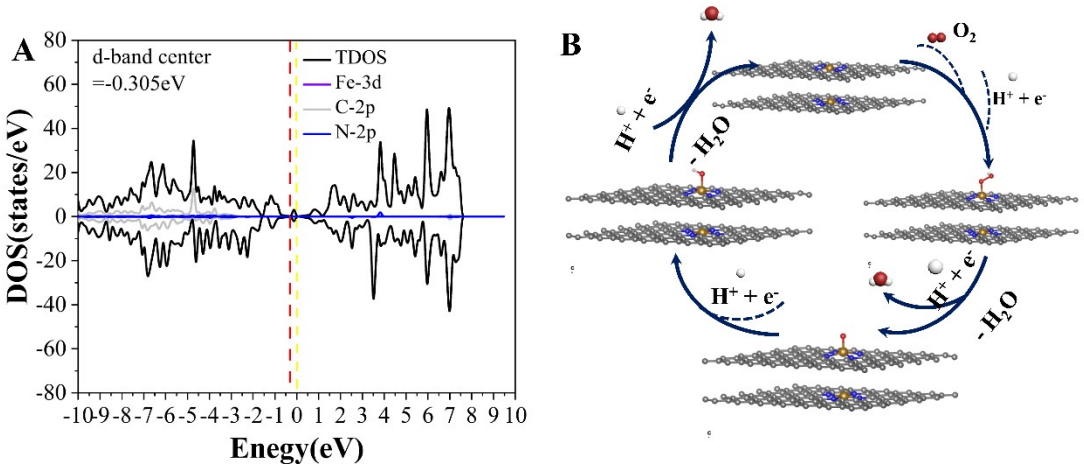

Fig. S20 The density of state of single lauer FeN_4 (A) and the ORR catalytic cycle path on duble layer FeN_4 (B).

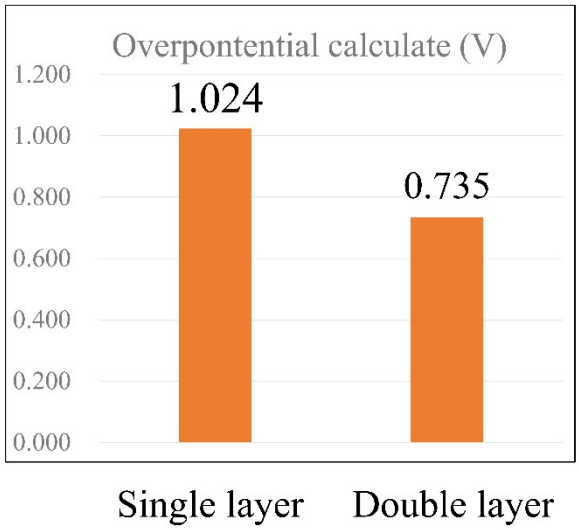

Fig. S21 The overpotential calculated from DFT simulation reveal that the overpotential for doulbe layer active center exhibit significantly lower overpotential in comparison to single layer.

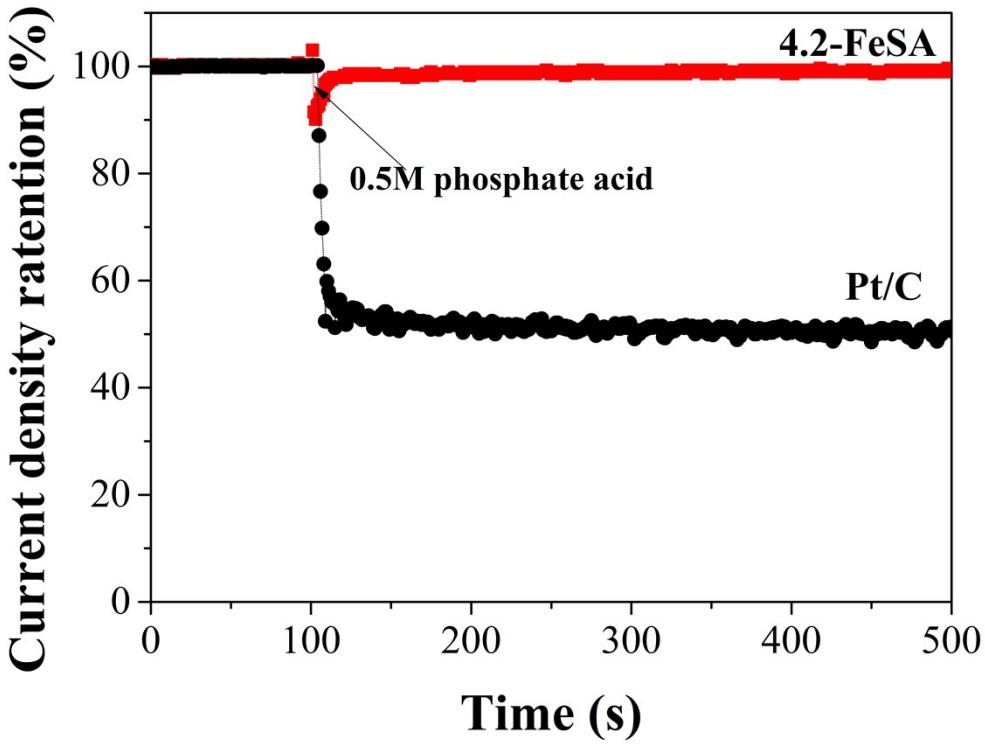

Fig. S22 Current density retention curves of 4.2-FeSA and Pt/C at 0.3 V in 0.1 m $HClO_4$ with re-addition of 0.5 M phosphate acid.

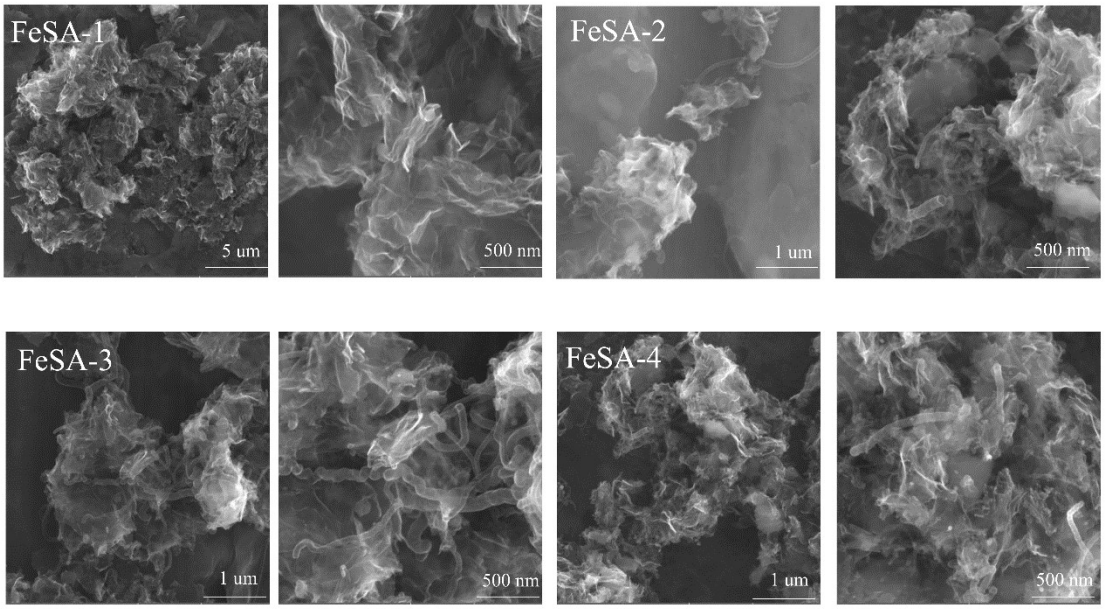

Fig. S23 The SEM image of FeSA through pyrolysis a blend of metal\nitrogen\carbon precursors (iron acetylacetonate, $C_2H_4N_4$ and graphene) with the same precursor amount of *x*-FeSA.

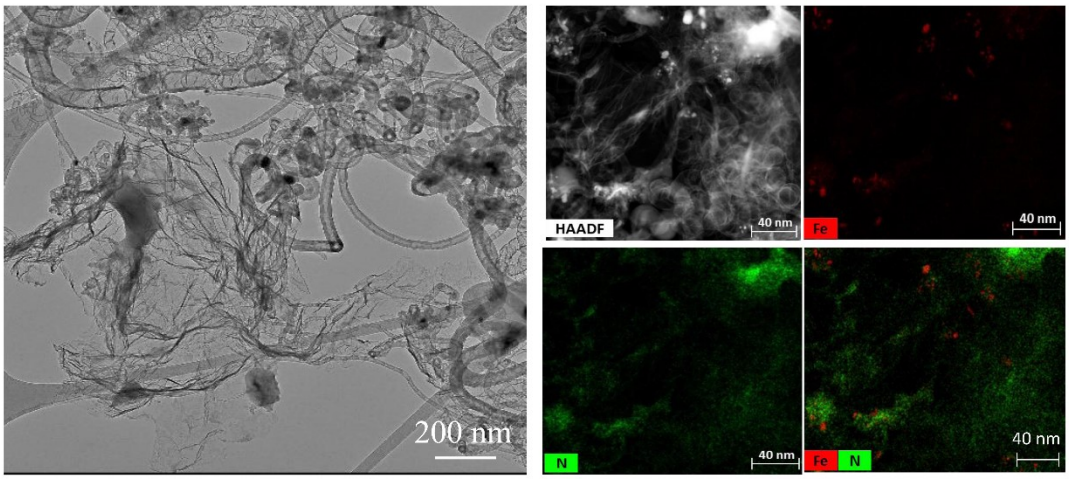

Fig. S24 The elemental mapping images and TEM image of FeSA-3.

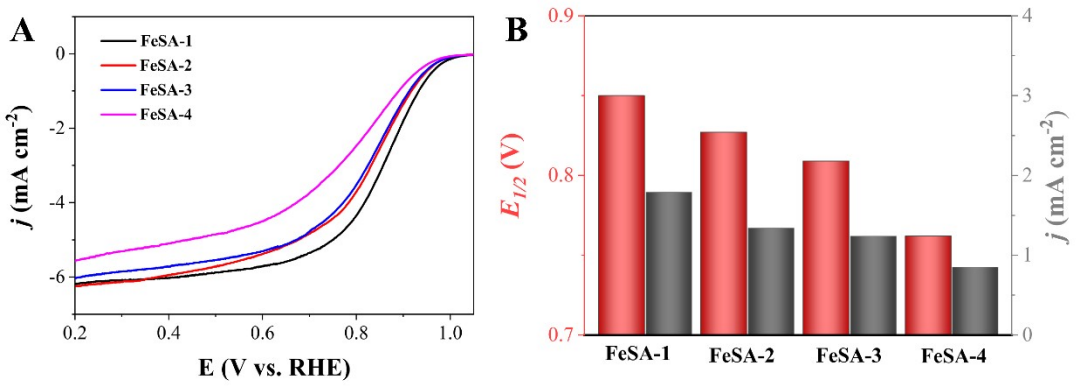

Fig. S25 The RDE polarization curves of Pt/C, FeSA-1, FeSA-2, FeSA-3 and FeSA-4 in 0.1 M KOH. Scan rate: 5 mV s^{-1} (A); comparison of the kinetic current density at 0.9V (J_k) and $E_{1/2}$ (B).

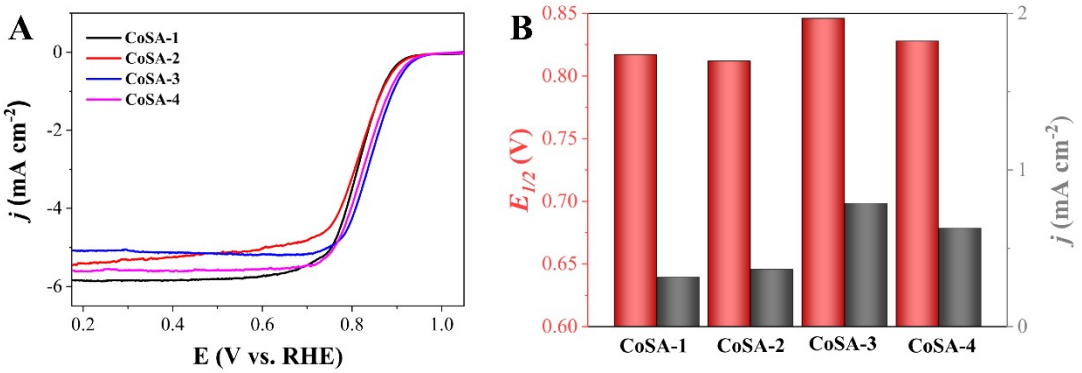

Fig. S26 The RDE polarization curves of Pt/C, CoSA-1, CoSA-2, CoSA-3 and CoSA-4 in 0.1 M KOH. Scan rate: 5 mV s^{-1} (A); comparison of the kinetic current density at 0.9V (J_k) and $E_{1/2}$ (B).

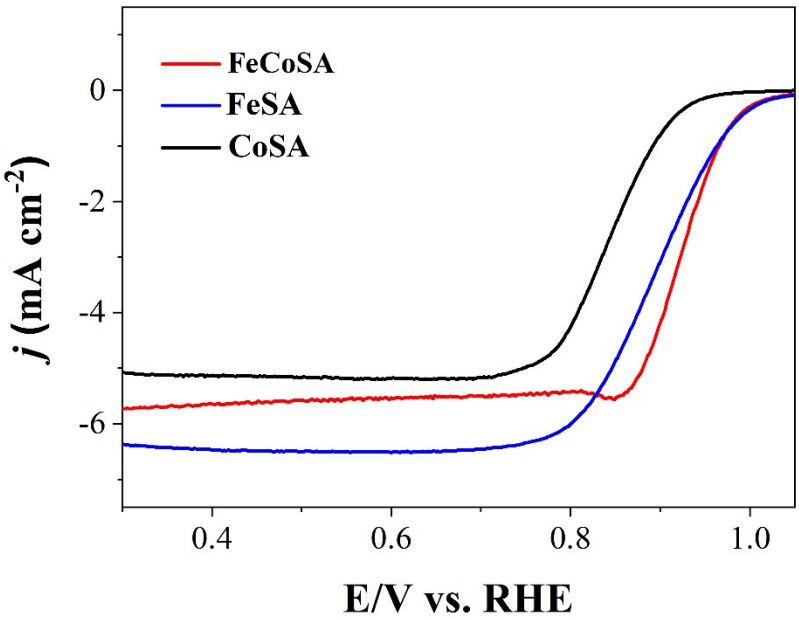

Fig. S27 The RDE polarization curves of FeSA, CoSA and FeCoSA in 0.1 M KOH. Scan rate: 5 mV s^{-1}

Table S1. The Fe content of FeO*x*

Sample	Loading by ICP-OES
2.5-FeO*x*	2.5wt%
3.9-FeO*x*	3.9wt%
6.9-FeO*x*	6.9wt%
7.6-FeO*x*	7.6wt%

Table S2. The average thickness of graphene, 1.7-FeSA, 2.5-FeSA, 4.2-FeSA and 4.8-FeSA, and the Fe content of FeSA.

Sample	Average thickness of 30 sections (nm)	Loading by ICP-OES
Graphene	0.632857nm	
1.7-FeSA	0.801563nm	1.7wt%
2.5-FeSA	0.945nm	2.5wt%
4.2-FeSA	1.24333nm	4.2wt%
4.8-FeSA	1.47667nm	4.8wt%

Table S3. XPS elemental surface analysis.

Catalysts	pyridinic N (content %)	Fe-N (content %)	pyrrolic N (content %)	graphitic N (content %)	oxidized N (content %)
1.7-FeSA	41.93	0.58	24.98	22.509	9.997
2.5-FeSA	46.94	2.478	25.127	23.421	2.03
4.2-FeSA	48.746	4.717	14.596	26.411	5.528
4.8-FeSA	56.444	6.9	13.937	15.033	7.677

Table S4. Structural parameters of the samples obtained from EXAFS fitting.

Sample	Bond type	N	R (Å)	ΔE_0 (eV)	$\sigma^2 \times 10^3$ (Å^2)	R-factor
1.7-FeSA	Fe-N	3.5	2.07±0.02	12.7±3.8	17.0±1.0	0.0147
	Fe-C	2.2	2.47±0.03	10.8±5.7	12.1±3.1	
2.5-FeSA	Fe-N	3.6	1.97±0.01	3.7±6.3	28.9±1.5	0.0025
	Fe-Fe	1.0±0.1	2.48±0.01	13.0±3.0	5.4±13.5	
	Fe-C	1.7±0.3	2.64±0.01	4.2±2.6	5.4±13.5	
4.2-FeSA	Fe-N	3.7	2.02±0.01	8.1±9.0	28.5±2.7	0.0027
	Fe-Fe	0.9±0.2	2.48±0.01	14.6±5.2	4.6±1.9	
	Fe-C	1.8±0.5	2.64±0.01	5.5±4.3	4.6±1.9	

N, coordination number; R, distance between absorber and backscatter atoms; ΔE_0, inner potential correction to account for the difference in the inner potential between the sample and the reference compound. σ^2, Debye–Waller factor; S_0^2 fitting from Fe sample defined as 0.75.

Table S5 Structural parameters of the samples obtained from EXAFS fitting.

Sample	Bond type	N	R (Å)	ΔE_0 (eV)	$\sigma^2 \times 10^3$ (Å^2)	R-factor
6.9-FeO*x*	Fe-O	4.7±0.5	2.00±0.01	-2.8±1.3	6.9±1.8	0.0081
	Fe-Fe	4.3±1.0	3.09±0.01	-0.5±2.1	7.8±2.3	
4.2-FeSA-350℃ 3h	Fe-N	1.0	1.94±0.02	-30.6±9.6	4.2±1.7	0.014
	Fe-O	3.0	2.05±0.02	-6.1±2.8	4.2±1.7	
4.2-FeSA-650℃ 1h	Fe-/N	3.0	2.02±0.02	-2.2±5.3	6.9±2.0	0.014
	Fe-O	1.1	2.14±0.01	3.6±4.9	5.5±1.9	
4.2-FeSA-650℃ 3h	Fe-C/N	6.6±0.9	2.00±0.01	-2.1±1.6	10.8±2.3	0.013

N, coordination number; R, distance between absorber and backscatter atoms; ΔE_0, inner potential correction to account for the difference in the inner potential between the sample and the reference compound. σ^2, Debye–Waller factor; S_0^2 fitting from Fe sample defined as 0.85.

Table S6. Summary of various recently reported advanced ORR electrocatalysts in 0.1M KOH.

Materials	Loading (mg cm^{-2})	$E_{1/2}$ (V)	Metal loading (wt%)	Synthesis strategy	REF.
FeAB-O	0.2	0.9	/	Coordination chemistry	Nat. Commun. (2020)[8]
N/Fe-CG	0.17	0.86	/	Electrospinning based approach	Nano energy (2019)[9]
Cu/C	0.4	0.847	5.4 (Cu)	Unique confined self-initiated dispersing protocol	Nano energy (2019)[10]
Fe-SAs/NPS-HC	0.1	0.912	1.54 (Fe)	Novel MOF@polymer	Nat. Commun. (2018)[11]
A-CoPt-NC	0.262	0.96	1.72 (Co)/0.16 (Pt)	Metal–organic framework derived single-atom catalyst, electrochemically activation	J. Am. Chem. Soc. (2018) [12]
Cu SAs/N-C-900	0.102	0.87	1.9 (Co)	Ionic exchange	Small (2020)[13]
Co-pyridinic N-C	0.25	0.87	2.14 (Co)	Modification of a lysozyme-modified zeolitic imidazolate framework	Adv. Energy Mater. (2020)[14]
Fe/Mn-Nx-C	0.396	0.88	/	Metal ions adsorption, pyrolysis	Appl. Catal. B (2021)[15]
Fe_{SA}–N–C	0.28	0.891	1.76 (Fe)	Mixed-ligand strategy in MOF system	Angew. Chem. Int. Ed. (2018)[16]
SA-Fe/NHPC	0.1	0.87	/	Utilizing the biomass resources	Small (2017)[17]
Cu-SA/SNC	0.102	0.893	4.5 (Cu)	Atomic interfacial engineering	Energy Environ. Sci. (2019)[18]
Fe-N-C-1	0.5	0.88	5.64 (Fe)	Controlling the annealing rate of metal precursor at 1 °C/min	Angew. Chem. Int. Ed. (2019)[19]
CAN-Pc (Fe/Co)	0.2	0.84	10.7 (Fe/Co)	One-step ball milling method	Angew. Chem. Int. Ed. (2019)[20]
PSTA-Co-1000	0.142	0.878	/	Template-free approach to construct cross-linked polyphosphazene nano-spheres with tunable hollow structures	Angew. Chem. Int. Ed. (2020)[21]
Zn/CoN–C	0.2551	0.861	0.33 (Zn)/0.14 (Co)	Competitive complexation	Angew. Chem. Int. Ed. (2019)[22]
Fe-ISA/NC	0.51	0.896	0.947 (Fe)	Pyrrole–thiophene copolymer pyrolysis	Adv. Mater. (2018)[23]
FeSAs/NSC	0.2	0.87	0.87 (Fe)	Template-assisted method	J. Am. Chem. Soc. (2019)[24]
Fe SAs–N/C-20	0.408	0.909	0.2 (Fe)	Metal–organic framework derived single-atom catalyst	J. Am. Chem. Soc. (2018)[25]
Pt/NBF-ReS_2/Mo_2CT	0.204	0.911	1.26 (Pt)	Wet chemistry, pyrolysis	Energy Storage Mater. (2021)[26]

Fe_x/OES	0.4	0.85	0.11 (Fe)	Silica-mediated MOF-templated	Angew. Chem. Int. Ed. (2020)[27]
Co_1-N_3PS/HC	0.51	0.92	0.39 (Co)	Metal–organic framework derived single-atom catalyst	Angew. Chem. Int. Ed. (2021)[28]
4.2-FeSA	0.408	0.901	4.2	In-situ atomization of metal oxide nanoparticles	This work
FeCoSA	0.408	0.924	5.2 (Fe)/0.4 (Co)	In-situ atomization of metal oxide nanoparticles	This work

Table S7. Summary of single atom catalyzed in zinc-air batteries

Materials	Open circuit voltage (V)	Power density (mw cm^{-2})	Durability	REF.
4.2-FeSA	1.60	212	450h@5 mA cm^{-2} for 2200 cycles	This work
Co-POC	/	78	2 mA cm^{-2} for 25 cycles	Adv. Mater. (2019)[29]
Fe-N_4 SAs/NPC	/	232	36h@2 mA cm^{-2} for108 cycles	Angew. Chem. Int. Ed. (2018)[30]
CoSA+ Co_9S_8/HCNTS	1.45	177.33	5 mA cm^{-2} for 24h	Small (2020)[31]
N–Fe/N/C-CNT	1.35	102.7	5 mA cm^{-2} for 100 cycles	Angew. Chem. Int. Ed. (2017)[32]
NGM-Co	1.439	152	60h@2 mA cm^{-2} for 180 cycles	Adv. Mater. (2017)[33]
CoSA/N, S-HCS	1.5	173.1	320h@10 mA cm^{-2} for 1000 cycles	Adv. Energy Mater. (2020)[34]
Fe–NCCs	1.36	66	/	ACS Appl. Energy Mater. (2018) [35]
Fe/Ni-N_x/OC	1.525	148	/	Adv. Mater. (2020)[36]
CoN_4/NG	1.51	115	100h@10 mA cm^{-2}	Nano energy (2018)[37]
Fe SAs/MC (950)	1.521	/	100h@5 mA cm^{-2}	ACS Energy Lett. (2018)[38]
N-Mo-holey G	1.37	83	(Solid-State) 80h@2 mA cm^{-2} for 500 cycles	Appl. Catal. B (2020)[39]
CoSAs@NC	1.46	105.3	81.5h@10 mA cm^{-2} for 250 cycles	Angew. Chem. Int. Ed. (2019)[40]
Co-Co_3O_4@NAC	1.449	164	35h@5 mA cm^{-2}	Appl. Catal. B (2020)[41]
PCN-A@FeSA	/	185	/	J. Energ. Chem. (2021)[42]
Fe/N-G-SAC	/	120	10 mA cm^{-2} for 240 cycles	Adv. Mater. (2020)[43]
Fe-NSDC	1.52	225.1	66.5h@4 mA cm^{-2} for 400 cycles	Small (2019)[44]
Co/Co–N–C	1.41	132	/	Adv. Mater. (2019)[45]
EA-Co-900	1.37	73	100h@20 mA cm^{-2}	Appl. Catal. B (2019)[46]
Co-N, B-CSC	1.43	100.4	14h@5 mA cm^{-2} for 128 cycles	ACS Nano (2018)[47]
Fe–N_x–C	1.51	96.4	10 mA cm^{-2} for 2000 min	Adv. Funct. Mater. (2019)[48]
NC-Co SA	1.411	20.9	(Solid-State) 2500 min,125	ACS Catal. (2018)[49]

NGM-Co	1.439	28.5	cycles (Solid-State) 1h@1mA cm^{-2} for	Adv. Mater. (2017)[33]
4.2-FeSA	1.43	112	18 cycles (Solid-State) 60h@2 mA cm^{-2}	This work

Table S8. The value of site density and turnover

Sample	SD (umol g^{-1})	TOF (s^{-1})	
		0.95V	**0.9V**
1.7-FeSA	27.66	0.61	2.32
2.5-FeSA	29.65	0.76	2.80
4.2-FeSA	31.25	1.05	3.57
4.8-FeSA	30.45	1.31	3.75

Table S9. Summary of power density in HT-PEMFCs

Materials	Power density ($mW\ cm^{-2}$)	REF.
PBI-Fe/C	60	J. Mater. Chem. A (2015)[50]
BP-FeNC	189.2	Appl. Catal. B (2018)[51]
Pt-Ru/MWCNT-GNP	280	Int. J. Energy Res.(2019)[52]
Pt/SiCTiC	227.4	Appl. Catal. B (2016)[53]
FeSA-G	276	Adv. Sci. (2019)[54]
Pt/FeP/C	465	Adv. Funct. Mater. (2021)[55]
Cu-PtFe/NC	432.6	Adv. Funct. Mater. (2021)[56]
20% Pt/C	250	J. Power Sources (2009)[57]
10% Pt/C	320	J. Power Sources (2019)[58]
4.2-FeSA	351.1	This work

Reference:

1. X. Wan, X. Liu, Y. Li, R. Yu, L. Zheng, W. Yan, H. Wang, M. Xu and J. Shui, *Nature Catalysis*, 2019, **2**, 259-268.
2. G. Kresse and J. Furthmüller, *Computational materials science*, 1996, **6**, 15-50.
3. G. Kresse and J. Furthmüller, *Physical review B*, 1996, **54**, 11169.
4. J. P. Perdew, K. Burke and M. Ernzerhof, *Physical review letters*, 1996, **77**, 3865.
5. G. Kresse and D. Joubert, *Physical Review B*, 1999, **59**, 1758-1775.
6. H. J. Monkhorst and J. D. Pack, *Physical review B*, 1976, **13**, 5188.
7. Y. Cheng, *Electrochimica Acta*, 2013, **99**, 124-132.
8. K. Chen, K. Liu, P. An, H. Li, Y. Lin, J. Hu, C. Jia, J. Fu, H. Li and H. Liu, *Nature communications*, 2020, **11**, 1-8.
9. B. Li, S. P. Sasikala, D. H. Kim, J. Bak, I.-D. Kim, E. Cho and S. O. Kim, *Nano Energy*, 2019, **56**, 524-530.
10. G. Han, Y. Zheng, X. Zhang, Z. Wang, Y. Gong, C. Du, M. N. Banis, Y.-M. Yiu, T.-K. Sham and L. Gu, *Nano Energy*, 2019, **66**, 104088.
11. Y. Chen, S. Ji, S. Zhao, W. Chen, J. Dong, W.-C. Cheong, R. Shen, X. Wen, L. Zheng and A. I. Rykov, *Nature communications*, 2018, **9**, 1-12.
12. L. Zhang, J. M. T. A. Fischer, Y. Jia, X. Yan, W. Xu, X. Wang, J. Chen, D. Yang, H. Liu, L. Zhuang, M. Hankel, D. J. Searles, K. Huang, S. Feng, C. L. Brown and X. Yao, *Journal of the American Chemical Society*, 2018, **140**, 10757-10763.
13. S. Ma, Z. Han, K. Leng, X. Liu, Y. Wang, Y. Qu and J. Bai, *Small*, 2020, **16**, 2001384.
14. Y. Ha, B. Fei, X. Yan, H. Xu, Z. Chen, L. Shi, M. Fu, W. Xu and R. Wu, *Advanced Energy Materials*, 2020, **10**, 2002592.
15. Z. Chen, X. Liao, C. Sun, K. Zhao, D. Ye, J. Li, G. Wu, J. Fang, H. Zhao and J. Zhang, *Applied Catalysis B: Environmental*, 2021, **288**, 120021.
16. L. Jiao, G. Wan, R. Zhang, H. Zhou, S.-H. Yu and H.-L. Jiang, *Angewandte Chemie International Edition*, 2018, **57**, 8525-8529.
17. Z. Zhang, X. Gao, M. Dou, J. Ji and F. Wang, *Small*, 2017, **13**, 1604290.
18. Z. Jiang, W. Sun, H. Shang, W. Chen, T. Sun, H. Li, J. Dong, J. Zhou, Z. Li, Y. Wang, R. Cao, R. Sarangi, Z. Yang, D. Wang, J. Zhang and Y. Li, *Energy & Environmental Science*, 2019, **12**, 3508-3514.
19. J. Li, S. Chen, N. Yang, M. Deng, S. Ibraheem, J. Deng, J. Li, L. Li and Z. Wei, *Angewandte Chemie International Edition*, 2019, **58**, 7035-7039.
20. S. Yang, Y. Yu, M. Dou, Z. Zhang, L. Dai and F. Wang, *Angewandte Chemie International Edition*, 2019, **58**, 14724-14730.
21. X. Wei, D. Zheng, M. Zhao, H. Chen, X. Fan, B. Gao, L. Gu, Y. Guo, J. Qin, J. Wei, Y. Zhao and G. Zhang, *Angewandte Chemie International Edition*, 2020, **59**, 14639-14646.
22. Z. Lu, B. Wang, Y. Hu, W. Liu, Y. Zhao, R. Yang, Z. Li, J. Luo, B. Chi, Z. Jiang, M. Li, S. Mu, S. Liao, J. Zhang and X. Sun, *Angewandte Chemie International Edition*, 2019, **58**, 2622-2626.

23. Q. Li, W. Chen, H. Xiao, Y. Gong, Z. Li, L. Zheng, X. Zheng, W. Yan, W. C. Cheong and R. Shen, *Advanced materials*, 2018, **30**, 1800588.
24. J. Zhang, Y. Zhao, C. Chen, Y.-C. Huang, C.-L. Dong, C.-J. Chen, R.-S. Liu, C. Wang, K. Yan, Y. Li and G. Wang, *Journal of the American Chemical Society*, 2019, **141**, 20118-20126.
25. R. Jiang, L. Li, T. Sheng, G. Hu, Y. Chen and L. Wang, *Journal of the American Chemical Society*, 2018, **140**, 11594-11598.
26. M. Yi, N. Li, B. Lu, L. Li, Z. Zhu and J. Zhang, *Energy Storage Materials*, 2021, **42**, 418-429.
27. C. C. Hou, L. Zou, L. Sun, K. Zhang, Z. Liu, Y. Li, C. Li, R. Zou, J. Yu and Q. Xu, *Angewandte Chemie International Edition*, 2020, **59**, 7384-7389.
28. Y. Chen, R. Gao, S. Ji, H. Li, K. Tang, P. Jiang, H. Hu, Z. Zhang, H. Hao and Q. Qu, *Angewandte Chemie International Edition*, 2021, **60**, 3212-3221.
29. B. Q. Li, C. X. Zhao, S. Chen, J. N. Liu, X. Chen, L. Song and Q. Zhang, *Advanced materials*, 2019, **31**, e1900592.
30. Y. Pan, S. Liu, K. Sun, X. Chen, B. Wang, K. Wu, X. Cao, W.-C. Cheong, R. Shen, A. Han, Z. Chen, L. Zheng, J. Luo, Y. Lin, Y. Liu, D. Wang, Q. Peng, Q. Zhang, C. Chen and Y. Li, *Angewandte Chemie International Edition*, 2018, **57**, 8614-8618.
31. Y. Li, R. Cao, L. Li, X. Tang, T. Chu, B. Huang, K. Yuan and Y. Chen, *Small*, 2020, **16**, 1906735.
32. P. Chen, T. Zhou, L. Xing, K. Xu, Y. Tong, H. Xie, L. Zhang, W. Yan, W. Chu, C. Wu and Y. Xie, *Angewandte Chemie*, 2017, **56**, 610-614.
33. C. Tang, B. Wang, H. F. Wang and Q. Zhang, *Advanced materials*, 2017, **29**, 1703185.
34. Z. Zhang, X. Zhao, S. Xi, L. Zhang, Z. Chen, Z. Zeng, M. Huang, H. Yang, B. Liu and S. J. Pennycook, *Advanced Energy Materials*, 2020, **10**, 2002896.
35. N. Jia, Q. Xu, F. Zhao, H.-X. Gao, J. Song, P. Chen, Z. An, X. Chen and Y. Chen, *ACS Applied Energy Materials*, 2018, **1**, 4982-4990.
36. Z. Zhu, H. Yin, Y. Wang, C. H. Chuang, L. Xing, M. Dong, Y. R. Lu, G. Casillas-Garcia, Y. Zheng and S. Chen, *Advanced Materials*, 2020, **32**, 2004670.
37. L. Yang, L. Shi, D. Wang, Y. Lv and D. Cao, *Nano Energy*, 2018, **50**, 691-698.
38. Z. K. Yang, C.-Z. Yuan and A.-W. Xu, *ACS Energy Letters*, 2018, **3**, 2383-2389.
39. P. Du, K. Hu, J. Lyu, H. Li, X. Lin, G. Xie, X. Liu, Y. Ito and H.-J. Qiu, *Applied Catalysis B: Environmental*, 2020, **276**, 119172.
40. X. Han, X. Ling, Y. Wang, T. Ma, C. Zhong, W. Hu and Y. Deng, *Angewandte Chemie*, 2019, **58**, 5359-5364.
41. X. Zhong, W. Yi, Y. Qu, L. Zhang, H. Bai, Y. Zhu, J. Wan, S. Chen, M. Yang, L. Huang, M. Gu, H. Pan and B. Xu, *Applied Catalysis B: Environmental*, 2020, **260**, 118188.
42. X. Shi, Z. Pu, B. Chi, M. Liu, S. Yu, L. Zheng, L. Yang, T. Shu and S. Liao, *Journal of Energy Chemistry*, 2021, **59**, 388-395.
43. M. Xiao, Z. Xing, Z. Jin, C. Liu, J. Ge, J. Zhu, Y. Wang, X. Zhao and Z. Chen,

advance materials, 2020, **32**, 2004900.
44. J. Zhang, M. Zhang, Y. Zeng, J. Chen, L. Qiu, H. Zhou, C. Sun, Y. Yu, C. Zhu and Z. Zhu, *Small*, 2019, **15**, 1900307.
45. D. Ji, L. Fan, L. Li, S. Peng, D. Yu, J. Song, S. Ramakrishna and S. Guo, *Advanced Materials*, 2019, **31**, 1808267.
46. J. Zhao, R. Qin and R. Liu, *Applied Catalysis B: Environmental*, 2019, **256**, 117778.
47. Y. Guo, P. Yuan, J. Zhang, Y. Hu, I. S. Amiinu, X. Wang, J. Zhou, H. Xia, Z. Song, Q. Xu and S. Mu, *ACS nano*, 2018, **12**, 1894-1901.
48. J. Han, X. Meng, L. Lu, J. Bian, Z. Li and C. Sun, *Advanced Functional Materials*, 2019, **29**, 1808872.
49. W. Zang, A. Sumboja, Y. Ma, H. Zhang, Y. Wu, S. Wu, H. Wu, Z. Liu, C. Guan, J. Wang and S. J. Pennycook, *ACS Catalysis*, 2018, **8**, 8961-8969.
50. Y. Hu, J. O. Jensen, W. Zhang, S. Martin, R. Chenitz, C. Pan, W. Xing, N. J. Bjerrum and Q. Li, *Journal of Materials Chemistry A*, 2015, **3**, 1752-1760.
51. Y. Hu, J. O. Jensen, C. Pan, L. N. Cleemann, I. Shypunov and Q. Li, *Applied Catalysis B: Environmental*, 2018, **234**, 357-364.
52. G. U. Alpaydin, Y. Devrim and C. O. Colpan, *International journal of energy research*, 2019, **43**, 3578-3589.
53. J. Lobato, H. Zamora, J. Plaza, P. Cañizares and M. A. Rodrigo, *Applied Catalysis B: Environmental*, 2016, **198**, 516-524.
54. Y. Cheng, S. He, S. Lu, J. P. Veder, B. Johannessen, L. Thomsen, M. Saunders, T. Becker, R. De Marco and Q. Li, *Advanced science*, 2019, **6**, 1802066.
55. S. Du, Y. Li, X. Wu, G. Huang, Y. Wu, J. Zhang, J. Zhang, S. Lu, Y. Cheng and L. Tao, *Advanced Functional Materials*, 2021, 2106758.
56. W. Li, D. Wang, T. Liu, L. Tao, Y. Zhang, Y. C. Huang, S. Du, C. L. Dong, Z. Kong and Y. f. Li, *Advanced Functional Materials*, 2021, 2109244.
57. C. Wannek, W. Lehnert and J. Mergel, *Journal of Power Sources*, 2009, **192**, 258-266.
58. D. Yao, W. Zhang, Q. Ma, Q. Xu, S. Pasupathi and H. Su, *Journal of Power Sources*, 2019, **426**, 124-133.